LASER & PHOTONICS REVIEWS
www.lpr-journal.org

# Novel High-Resolution and Large-Bandwidth Micro-Spectrometer Using Multi-Input Counter-Propagating Arrayed Waveguide Grating and Dual-Wavelength Grating Coupler on Silicon on Insulator

*Jun Zou,* Lingfeng Li, Changhui Wang, Yuan Zhuang,* Xuyang Wang, Jinhua Hu, Shaobo Luo,* and Jian-Jun He**

**Miniaturized micro-spectrometers with high-resolution and large-bandwidth are of great importance for on-site spectroscopic analysis applications. Here, a novel high-resolution and large-bandwidth micro-spectrometer is presented, which operates at dual-wavelength band by utilizing a $(N + 3) \times (N + 3)$ arrayed waveguide grating (AWG) and three dual-wavelength grating couplers on a silicon-on-insulator (SOI) platform. The AWG working in a counter-propagating manner can be viewed as two $3 \times N$ AWGs, and the dual-wavelength grating coupler acts as a prefilter. Three time-division-multiplexing inputs with wavelength spacings of 4/3 times that of $N$ output waveguides are employed to improve the resolution of the micro-spectrometer. Combining the corresponding outputs of three inputs, a micro-spectrometer with resolution enhanced to one-third wavelength spacing of output waveguides and effective channel number enlarged to $3 \times (N - 2)$ is achieved, only using $N$ output channels at each wavelength band. A micro-spectrometer with 63 effective channels and resolutions of 0.5 and 0.442 nm at 1550 and 1310 nm bands, respectively, is experimentally demonstrated. The footprint of the fabricated micro-spectrometer is $2 \times 0.81$ mm$^2$, with measured on-chip losses of −4.6 to −2.8 dB (−7.0 to −3.1 dB) and crosstalk levels < −18.5 (−16.8) dB at the 1550 (1310) nm band.**

## 1. Introduction

Spectroscopic detection, by means of the absorption or reflection of light,[1–3] is an essential method to discern and quantify various substances based on their unique "fingerprints." However, conventional benchtop spectrometers are usually very bulky and expensive, not suitable to on-site spectroscopic analysis where spectrometers with small size, low cost, and low power consumption are highly desired. In recent years, planar-waveguide-based on-chip spectrometers,[4,5] which have the advantages of ultracompact size and capabilities of monolithically integrated with light sources, detectors, and microfluidic units on a same chip,[6–9] have been drawing numerous research interests because of the potential use in miniaturized spectrum detection systems for applications to food ingredients detection,[10] medical diagnosis,[11] and industrial and agricultural production.[12] More attracting

J. Zou, L. Li, C. Wang
College of Science
Zhejiang University of Technology
Hangzhou 310023, China
E-mail: zoujun@zjut.edu.cn

Y. Zhuang
Zhejiang Lab
Hangzhou 311106, China
E-mail: zhuangyuan@zhejianglab.com

X. Wang
State Key Laboratory of Quantum Optics and Quantum Optics Devices
Shanxi University
Taiyuan 030006, China

J. Hu
School of Information & Electronic Engineering
Hebei University of Engineer
Handan 056038, China

S. Luo
School of Microelectronics
Southern University of Science and Technology
Guangdong Province 518055, China
E-mail: luos@u.nus.edu

J.-J. He
State Key Laboratory of Modern Optical Instrumentation
Centre for Integrated Optoelectronics
College of Optical Science and Engineering
Zhejiang University
Hangzhou 310027, China
E-mail: jjhe@zju.edu.cn

The ORCID identification number(s) for the author(s) of this article can be found under https://doi.org/10.1002/lpor.202200355

DOI: 10.1002/lpor.202200355

thing is that the mass production of on-chip spectrometers can be achieved with low cost by employing the well-established complementary metal-oxide-semiconductor (CMOS) fabrication technology.

In planar-waveguide-based spectrometers, light is routed and collected through either a Fourier-transform interferometer array (Fourier transform spectrometers, FTSs)[4,13–18] or a wavelength separating element.[19–28] Most FTSs employ an array of Mach–Zehnder interferometers (MZIs) with linearly increased path length differences[13–15] (also called spatial heterodyne FTSs, SH-FTSs). Although they have the benefit of high optical throughput, there is a tradeoff between spectral bandwidth and resolution due to the limited number of MZIs on a chip. In order to address this issue, FTSs could be implemented by using a balanced MZI with one tunable arm via the thermo-optic effect[16,17] or electro-optic effect.[18] However, these two effects are only suited for specific material platforms, and, on the other hand, new issues such as high power consumption and long measurement time raise. Moreover, the high heating power also induces nonlinearity and measuring stability issues, complicating the testing system. A wavelength separating element is mainly based on a microring resonator array[19–21] or a dispersive grating such as planar concave gratings (PCGs)[22,23] and arrayed waveguide gratings (AWGs).[24–28] Usually, a ring resonator is very susceptible to fabrication errors, and it is very difficult to have uniform wavelength separation for a ring resonator array. PCGs have the advantage of ultracompact size, but it is very challenging to fabricate high-quality grating facets. AWGs are one of fundamental building blocks in photonic integrated circuits and widely used in wavelength division multiplexing communication systems owing to their high stability, scalability of channels, and good spectral uniformity.[29] On-chip spectrometers based on AWGs have extensively been investigated and demonstrated.[24–26,28] However, the size of AWG spectrometer increases significantly as the spectral resolution improves. Even worse, due to fabrication imperfections such as width fluctuation, sidewall roughness, and film thickness nonuniformity in waveguide core, spectral performance of AWGs also deteriorates substantially with increasing footprint of phase regions consisting of phased array waveguides and slab waveguides, especially for AWG-based spectrometers on high-index-contrast material platforms. Hence, it is very difficult to keep an ultracompact size to maintain good spectral performance (i.e., low insertion loss and low crosstalk) for AWG spectrometers while having high resolution and large bandwidth. In recent years, a counter-propagating silicon AWG is proposed[30] and employed in a polarization-diversity wavelength demultiplexer[31,32] to process two orthogonal polarization components of input light, in an interleaved wavelength demultiplexer[33] to relax the degradation of spectral crosstalk due to fabrication imperfections, and in an interleaved wavelength multiplexer[34] to increase the channel bandwidth.

In this paper, we propose an ultracompact high-resolution and large-bandwidth on-chip spectrometer based on a $(N + 3) \times (N + 3)$ AWG and three dual-wavelength grating couplers. The designed AWG operates in a counter-propagating manner to support the wavelength separating at dual-wavelength band while the previously demonstrated conventional counter-propagating AWGs[31–34] only work at one wavelength band. The dual-wavelength input grating coupler acts as a prefilter to separate these two wavelength bands. For each wavelength band, the AWG operates at a different diffraction order, and there have three input ports and $N$ output ports. The wavelength spacing between output ports is set to $\Delta\lambda$ while that between input ports is designed to $4/3\ \Delta\lambda$. These three inputs are time-division-multiplexed, i.e., only one input is excited at a time. Combining the spectral responses of each input, we obtain a spectrometer with wavelength spacing decreased to one-third $\Delta\lambda$ and channel count of $3 \times (N - 2)$ in each wavelength band, while the footprint (phase region) of the designed AWG remains the same as that of the AWG with a wavelength spacing of $\Delta\lambda$ to keep a good spectral performance at each output channel. In an experiment, we demonstrated a spectrometer operating at dual-wavelength band by employing a $26 \times 26$ AWG and three dual-wavelength grating couplers working at 1550 and 1310 nm bands on the 220 nm SOI platform. For each wavelength band, the effective channel number is 63, and the wavelength spacings are 0.5 and 0.442 nm at 1550 and 1310 nm bands, respectively. Thanks to the ultracompact size of the designed AWG, low loss, and low nonadjacent crosstalk are achieved at each output channel for the fabricated spectrometer.

One of potential use cases of the designed spectrometer is in miniaturized fiber Bragg grating (FBG) sensor interrogation systems where a large number of FBGs need to be demodulated simultaneously. Compared to the conventional AWG-based interrogators (usually at least two adjacent output channels are needed for one FBG[35,36]) for a given number of FBG sensors, the designed spectrometer has more compact size and can substantially reduce the required number of output channels (photodetectors) due to the working principle of time division multiplexing, which decreases the complexity of the whole interrogation system (including assembly and circuit design) and in turn the cost. Especially for tens, hundreds, or thousands of FBGs, the dual-wavelength band can be fully used, and the advantage would be more obvious. Another use case is miniaturized spectral-domain optical coherence tomography (SD-OCT) systems[37,38] where a high-resolution and large-bandwidth spectrometer is one of the key components and the proposed spectrometer can be designed for this application. In addition, multiple proposed spectrometers with different dual wavelengths can be parallelly utilized to expand the working wavelength range for spectral tissue sensing applications,[24] and one input or three time-division-multiplexing inputs can be properly selected according to resolution requirement.

## 2. Principle and Design

### 2.1. Principle

**Figure 1** shows the schematic diagram of the proposed micro-spectrometer employing a $(N + 3) \times (N + 3)$ AWG and three dual-wavelength grating couplers. Usually, a typical AWG consists of single input waveguide, free propagation regions 1 and 2 (FPR 1 and FPR 2), phased array waveguides with a length difference of $\Delta L$ between consecutive array waveguides, and an array of output waveguides. In our proposed AWG structure, there have both three input waveguides and $N$ output waveguides connecting to each FPR. And all three input waveguides are connected to three dual-wavelength grating couplers, respectively. For easy

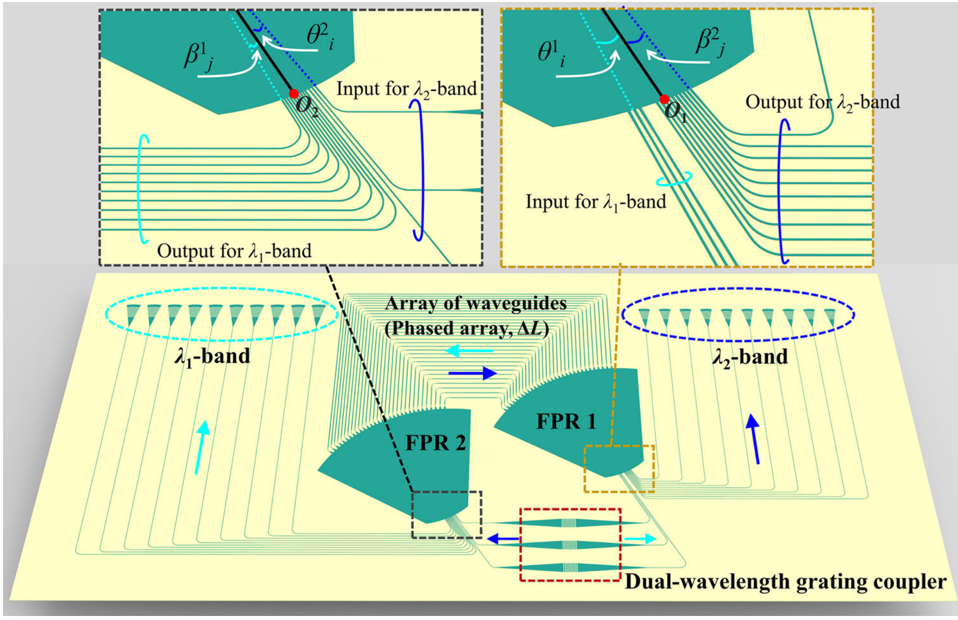


**Figure 1.** Schematic diagram of the proposed micro-spectrometer based on a $(N+3)\times(N+3)$ AWG and three dual-wavelength grating couplers.

understanding, the AWG can be viewed as two $3\times N$ AWGs with each one corresponding to one wavelength band. The dual-wavelength grating coupler can couple and split light in dual-wavelength band ($\lambda_1$ and $\lambda_2$ bands) from optical fiber into two separate waveguides simultaneously. The micro-spectrometer works as follows: light from an optical fiber is first coupled into one of the three dual-wavelength grating couplers, with $\lambda_1$ band being routed to the right-side input and $\lambda_2$ band to the left-side input. The $\lambda_1$-band light enters and diffracts at FPR 1, then is coupled into the phased array waveguides. Subsequently, all sub-beams from each phased array waveguide interfere at FPR 2 and refocus onto $N$ output waveguides depending on wavelength. Finally, an array of single-wavelength grating couplers working at $\lambda_1$-band is employed to couple out all separated wavelength signals to detectors. Similarly, the $\lambda_2$-band light propagates in the opposite direction and refocuses at FPR 1 to separate all wavelength signals. The channel spacing of the three input waveguides is designed to be 4/3 times that of $N$ output waveguides at each wavelength band. Since the spectral response of AWG has periodic characteristic, the $\lambda_1$ and $\lambda_2$ bands can share the common $(N+3)\times(N+3)$ AWG but work at a different grating diffraction order. The grating equation for these dual-wavelength bands can be expressed as

$$n^k_{\mathrm{s\_}ij} d_\mathrm{a} \sin\theta^k_i + n^k_{\mathrm{a\_}ij}\Delta L + n^k_{\mathrm{s\_}ij} d_\mathrm{a}\sin\beta^k_j = m^k\,\lambda^k_{i\_j}$$
$$(i=1,2,3;\ j=1,2,\ldots,N-1,N) \tag{1}$$

where $k=1$ represents the $\lambda_1$ band and $k=2$ represents the $\lambda_2$ band. $m^k$ is an integer diffraction order, and subscripts $i$ and $j$ denote input waveguide number and output waveguide number, respectively. $\lambda^k{}_{i\_j}$ denotes the central wavelength at the $j$th output waveguide for the $i$th input waveguide. $n^k{}_{\mathrm{s\_}ij}$ and $n^k{}_{\mathrm{a\_}ij}$ are the effective indices of the free propagation region and phased array waveguides, respectively, at $\lambda^k{}_{i\_j}$. $d_\mathrm{a}$ is a constant projection period of the end points of phased array waveguides on the tangent line at the grating pole.[39] $\theta^k{}_i$ is the angle between the $i$th input waveguide and the central axis of the free propagation region, and $\beta^k{}_j$ is the angle between the $j$th output waveguide and the central axis of the free propagation region, as shown in the inset of Figure 1.

In the proposed $(N+3)\times(N+3)$ AWG, the three inputs at each wavelength band are time-division-multiplexed, i.e., only one input is excited at a time. For each input, there corresponds to $N$ separated output wavelengths denoted as $\lambda_{i\_1}, \lambda_{i\_2}, \ldots, \lambda_{i\_N-1}, \lambda_{i\_N}$ with the wavelength spacing of $\Delta\lambda$. Since the wavelength spacing between input waveguides is designed to 4/3 $\Delta\lambda$, there are wavelength offsets of 4/3 $\Delta\lambda$ and 8/3 $\Delta\lambda$ for the second input ($i=2$) and third input ($i=3$), respectively, for the spectral responses at $N$ output waveguides, as compared to the first input ($i=1$). By combining all spectral responses of these three inputs, we can obtain a new wavelength group with the wavelength spacing of 1/3 $\Delta\lambda$ and the effective channel number of $3\times(N-2)$, as illustrated in **Figure 2**.

### 2.2. Dual-Wavelength Grating Coupler Design

The input dual-wavelength grating coupler is designed to couple and split the light of 1550 ($\lambda_1$) and 1310 ($\lambda_2$) nm wavelength bands into different input waveguides simultaneously while the output grating coupler is only designed to couple the light of 1550 or 1310 nm band out of waveguides. The dual-wavelength grating coupler was first proposed by Roelkens et al.[40] and demonstrated in ref. [41]. A new demonstration of the dual-waveguide grating coupler is in ref. [42], with a low fabrication cost by using 193 nm lithography. Here a dual-wavelength grating coupler with lower losses (3.35 dB at the designed wavelength 1310 nm and 4.52 dB at 1550 nm, with 1.55 and 0.68 dB improvements, respectively, over ref. [42]) and more compact footprint is reported. **Figure 3**a

 

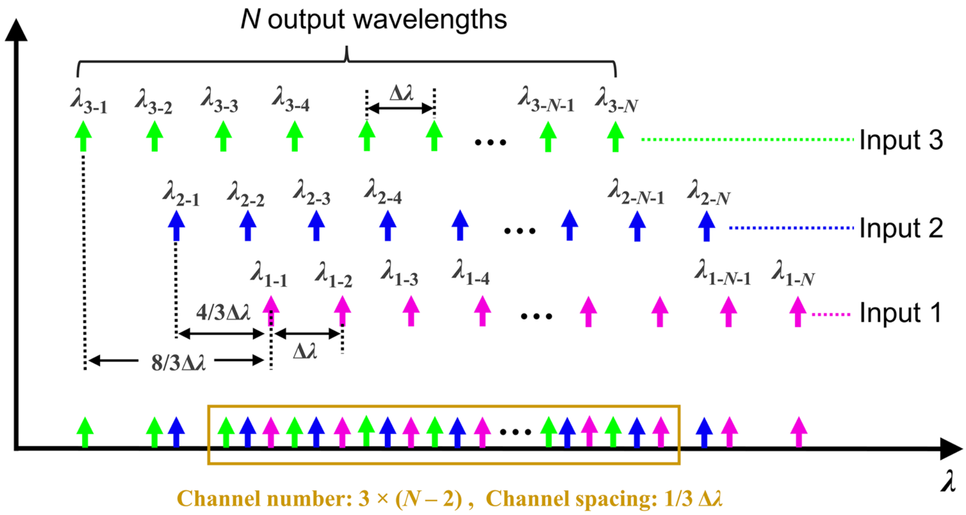


**Figure 2.** Illustration of combining spectral responses of all three inputs to produce a new wavelength group with a uniform wavelength spacing of 1/3 $\Delta\lambda$ and an effective channel number of $3 \times (N-2)$.

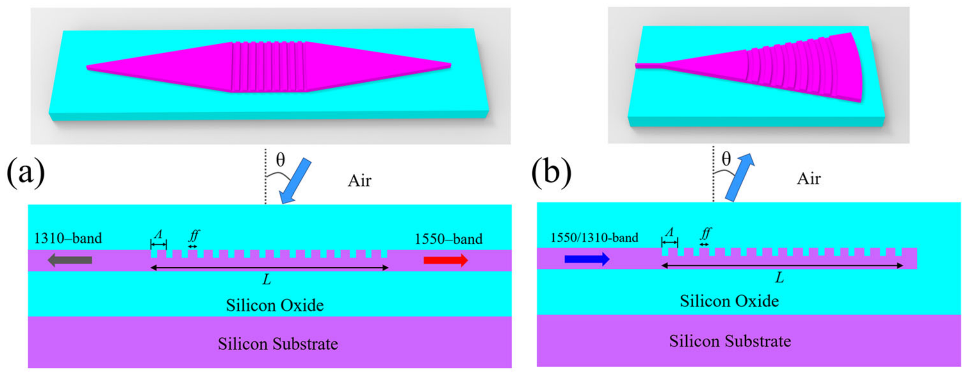


**Figure 3.** Schematic diagram of a) the dual-wavelength grating coupler working at 1550 and 1310 nm band and b) the conventional single-wavelength grating coupler operating at 1550 or 1310 nm band.

shows the cross section of the dual-wavelength grating coupler, as well as the cross section of a conventional single-wavelength grating coupler working only at 1550 or 1310 nm wavelength band. In order to couple the 1550 and 1310 nm wavelength bands into the right and left waveguides, respectively, the grating equations for 1550 and 1310 nm wavelengths should be satisfied simultaneously in the dual-wavelength grating coupler and are written as[40]

$$\Lambda(n_{e\_1.55} + n_{air} \sin \theta) = 1.55 \tag{2}$$

$$\Lambda(n_{e\_1.31} - n_{air} \sin \theta) = 1.31 \tag{3}$$

with $n_e$ being the effective index of guiding mode in the grating region, $n_{air}$ the refractive index of air, $\Lambda$ (in µm) the grating period, and $\theta$ the input angle of optical fiber in air. $n_e$ is dependent on the duty cycle $ff$ ($ff = L_{unetched}/\Lambda$, $L_{unetched}$ is the unetched length within one grating period) and etch depth $d_{etch}$ of the grating region. Here the employed SOI wafer has a top silicon layer thickness of 220 nm and buried oxide (BOX) layer with a thickness of 2 µm. Considering fabrication tolerance and the minimum feature size required in deep ultraviolet (DUV) lithography, we set $ff = 0.5$ and grating etch depth $d_{etch} = 70$ nm, which is the same as the used single-wavelength grating coupler at output ports, and the designed polarization is transverse electric (TE) polarization. Then we assume $n_e = ff \times n_{e\_unetched} + (1 - ff) \times n_{e\_etched}$, with $n_{e\_unetched}$ and $n_{e\_etched}$ being the effective indices of the unetched and etched parts of grating facet, respectively. $n_{e\_unetched}$ and $n_{e\_etched}$ can be approximated as the effective indices of 1D slab waveguides with thicknesses of 220 and 150 nm, respectively, since the width of the grating coupler is typically 10 µm, which is much larger than the operating wavelength. As a result, we can easily derive $n_{e\_1.55} = 2.6935$ and $n_{e\_1.31} = 2.8490$ for TE polarization. **Figure 4** shows the relationship between $\Lambda$ and $\theta$ for the wavelengths of 1550 and 1310 nm, respectively. It is known that as $\theta = 18°$ and $\Lambda = 0.516$ µm, both Equations (2) and (3) are satisfied simultaneously. On the other hand, the length $L$ of the grating region should be appropriately set to achieve high coupling efficiency for both 1550 and 1310 nm wavelengths. Considering that the mode field diameters of single-mode optical fiber are around 10.5 and 9.2 µm at 1550 and 1310 nm, respectively, we select the number of grating periods to be 19.5, i.e., $L = 19.5 \times 0.516 = 10.062$ µm, at

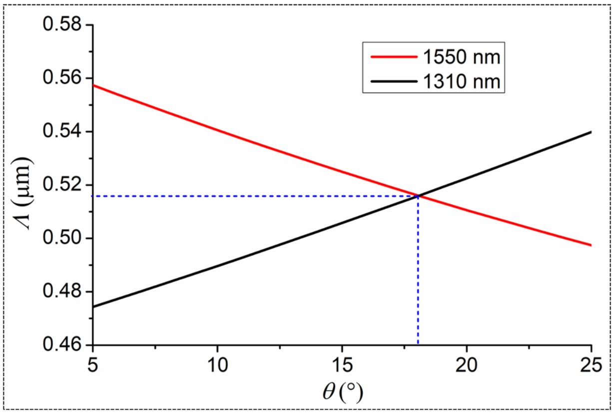


**Figure 4.** Grating period Λ versus input angle $\theta$ of optical fiber in air, for the 1550 and 1310 nm bands, respectively.

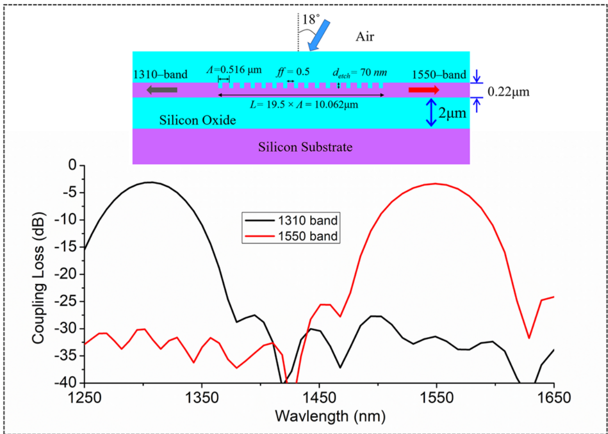


**Figure 5.** Calculated coupling efficiencies at 1550 and 1310 nm bands, respectively, for the designed dual-wavelength grating coupler, by using 2D FDTD simulation. The optical fiber is located at the center of the grating region in the simulation.

the grating region. The footprint of the designed dual-wavelength grating coupler is 250 (including two taper lengths of 120 μm) × 10 μm$^2$, more than six times smaller than the recently demonstrated dual-wavelength grating coupler.[42] **Figure 5** shows calculated coupling efficiencies for the 1550 and 1310 nm bands with key parameters of the grating region indicated, by using 2D finite difference time domain (FDTD) simulation. The calculated peak coupling efficiencies are around −3.1 and −3.4 dB for the 1310 and 1550 nm bands, respectively, and the cross talk is better than 20 dB within the 3 dB bandwidth of each wavelength band. The employed single-wavelength grating coupler at output ports has a grating period of Λ = 0.62 μm and $\theta = 10°$ for the 1550 nm band and Λ = 0.489 μm and $\theta = 10°$ for the 1310 nm band.

### 2.3. (*N*+3) × (*N*+3) AWG Design

A 26 × 26 AWG is designed based on the SOI platform with the 220 nm thick top silicon layer. At 1550 nm wavelength band, 23 output channels are designed to have a channel spacing of 1.5 nm, which determines a channel spacing of 2.0 nm for the corresponding three input channels, while at 1310 nm wavelength band, we keep the same pitch between output waveguides as that at 1550 nm band, hence the 23 output channels are designed to have a channel spacing of 1.327 nm determining a channel spacing of 1.769 nm for the corresponding three input channels. In order to reduce the sensitivity of effective index of waveguide to width fluctuation originating from fabrication imperfections, each waveguide in the phased array is designed to consist of broad straight waveguide with a width of 800 nm, narrow bending waveguide with a width of 400 nm, and adiabatic tapers with a length of 6 μm to connect the broad and narrow waveguides. The width of 400 nm meets single-mode propagation for 1550 nm band, while nearly single-mode propagation for 1310 nm band. For the layout design, the two star couplers (FPR 1 and FPR 2) are parallelly arranged with a tilted angle to keep the same total length of curved waveguides at each phased array waveguide; thus, the phase difference between consecutive array waveguides is only introduced by the broad waveguide. As reported in our previous research,[32] spectral performance of a typical AWG on the SOI platform is directly related to the size of its phase region (including FPR and phased array waveguides) which is mainly dependent on the radius $R$ of FPR. Using Equation (1), $R$ can be derived as

$$R = d_a d_o^k \times \frac{\lambda_o^k}{\Delta\lambda^k} \times \frac{n_s^k}{n_{ga}^k \Delta L + n_{gs}^k d_a \sin\theta_i^k} \tag{4}$$

where $n^k{}_{gs}$ and $n^k{}_{ga}$ are the group indices of FPR and phased array waveguide, respectively. $d^k{}_o$ is the output waveguide pitch at the interface between FPR and output waveguides, $\lambda^k{}_0$ and $\Delta\lambda^k$ are the designed central wavelength and channel spacing, respectively. Usually, $n^k{}_{gs}\, d_a \sin\theta^k{}_i \ll n^k{}_{ga}\,\Delta L$, hence $R$ is mainly proportional to the product of $d^k{}_o \times d_a$ for a given $\Delta\lambda^k$. In the current design, we set $d^k{}_o = 1.5$ μm for both 1550 and 1310 nm bands and $d_a = 2.5$ μm to make the phase region as compact as possible to achieve good spectral performance at each output channel. In order to reduce the coupling between adjacent output waveguides approaching FPR, a deeply etched receiving waveguide, i.e., a linear taper waveguide with an entrance width of 1 μm and an exit width of 0.43 μm for the 1550 nm band and a linear taper waveguide with the entrance width of 0.95 μm and the exit width of 0.38 μm for the 1310 nm band, is introduced between each output waveguide and FPR. A mode converter composed of a shallow etched multimode interference (MMI) coupler with a width of 2.3 μm and a length of 2.7 μm and a deeply etched parabolic taper with a length of 3.5 μm are inserted between FPR and each phased array waveguide, as illustrated in **Figure 6**a, to reduce the mode transition loss between FPR and phased array waveguides. The MMI coupler, on the one hand, couples the diffracted light from FPR and focuses it onto two spots at the end interface of MMI,[43] and, on the other hand, collects the diffracted light at shallow etched gaps between MMI couplers. The two focused spots excite the second-order and fundamental modes of the connected parabolic taper,[44] and the second-order mode is gradually coupled to the fundamental mode as the taper width decreases in the transmission direction. After propagating through the parabolic taper, the light is fully coupled to the fundamental mode of single-mode output waveguide. Using 3D FDTD simulation, the light transmissions between FPR (the fundamental

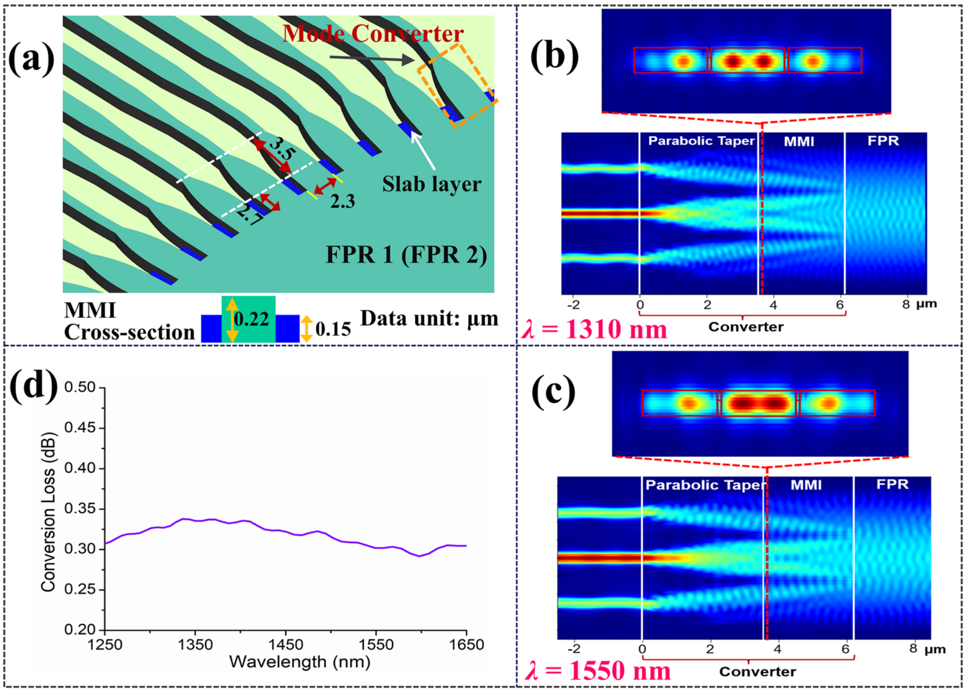


**Figure 6.** a) Structure of the introduced mode converters between FPR and phased array waveguides. b,c) The light transmission from FPR (the fundamental mode of FPR is used as the input light) to three output waveguides at b) 1310 nm and c) 1550 nm, with top insets showing the electric filed distribution at the end interface (marked with red dash line) of MMI couplers, and d) calculated mode conversion loss between FPR and phased array waveguides at 1250–1650 nm.

mode of FPR is used as the light input in the simulation) and three output waveguides at $\lambda = 1310$ and 1550 nm, respectively, are shown in Figure 6b,c. The top insets of Figure 6b,c give the electric field distribution at the end interface of MMI couplers (i.e., indicated by the red dash line) showing two focused spots at the end of each MMI. The mode conversion loss between FPR and phased array is calculated as small as 0.34 dB within a broadband wavelength range from 1250 to 1650 nm, as shown in Figure 6d. For the $N + 3$ waveguides at the interface of FPR 1, the $N$ output waveguides correspond to their three input waveguides at FPR 2 while the three input waveguides correspond to their $N$ output waveguides at FPR 2. Therefore, at the interfaces of FPR 1 and FPR 2, to avoid the overlapping between $N$ output waveguides and three input waveguides, the input angle $\theta^k{}_i$ of three input waveguides should satisfy the condition as follows

$$R \times \sin\theta_i^1 > d_o^2 \times \frac{N}{2} \tag{5}$$

$$R \times \sin\theta_i^2 > d_o^1 \times \frac{N}{2} \tag{6}$$

It should be pointed out that in the proposed AWG design, the off-center input is employed, which induces an excess loss compared with the conventional center input AWG design since all phased array waveguides on the grating circle are arranged to point at the center $O_1$ ($O_2$) of the interface between FPR 1 (FPR 2) and input/output waveguides, as shown in the inset of Figure 1. Hence $\theta^k{}_i$ should be appropriately set to decrease the excess loss. **Table 1** lists the main design parameters of the 26 × 26 AWG working at two wavelength bands. The footprint of the designed micro-spectrometer including all input and output waveguides is only $2 \times 0.81$ mm$^2$.

## 3. Fabrication and Characterization

### 3.1. Fabrication

The proposed micro-spectrometer is fabricated on an SOI wafer with a 220 nm thick top silicon layer and 2 μm thick BOX layer. First, the pattern of the micro-spectrometer is defined into a layer of photoresist (PR) by using 193 nm photolithography and transferred into the $SiO_2$ hard mask by means of inductively coupled plasma etching. Then a layer of 70 nm thick silicon is etched to form grating couplers and shallow-etched MMI-based mode converters. Subsequently, the remaining 150 nm thick silicon is fully etched to form input/output and phased array waveguides. Finally, an upper-cladding layer of $SiO_2$ with a thickness of 2 μm is deposited using plasma-enhanced chemical vapor deposition (PECVD). **Figure 7** shows optical microscope images of the fabricated micro-spectrometer, together with close-ups of key structures. Before measuring the spectral responses of the designed micro-spectrometer, we first test the performance of the dual-wavelength input grating coupler.

### 3.2. Characterization

Light from one tunable laser source with the wavelength ranging from 1260 to 1360 nm first passes through a fiber-based polarization controller which can adjust the polarization direction of

**Table 1.** Main design parameters of the 26 × 26 AWG.

| Parameter | 1550 nm band | | 1310 nm band |
|---|---|---|---|
| Array waveguide dimension [μm$^2$] | | 220 × 800 | |
| Narrow bending waveguide dimension [μm$^2$] | | 220 × 400 | |
| Central wavelength for the second input [nm] | 1550 | | 1310 |
| Output waveguide channel spacing [nm] | 1.5 | | 1.326 |
| Input waveguide channel spacing [nm] | 2.0 | | 1.768 |
| Angle $\theta^k{}_2$ for the second input [rad] | 0.082 | | 0.082 |
| Diffraction order $m$ | 19 | | 24 |
| Radius $R$ of FPR1 and FPR 2 [μm] | | 257.5 | |
| Delay length $\Delta L$ [μm] | | 10.735 | |
| Number of arrayed waveguides | | 91 | |
| Pitch $d_a$ between adjacent array waveguides on tangent line [μm] | | 2.5 | |
| Pitch $d^k{}_o$ at the interface between FPR1 (FPR2) and output waveguides [μm] | | 1.5 | |
| Input/output waveguide width $w$ [μm] | 0.43 | | 0.38 |
| Free spectral range (FSR) [nm] | 55.9 | | 39.7 |
| Footprint of the phase region [μm$^2$] | | 590 × 585 | |

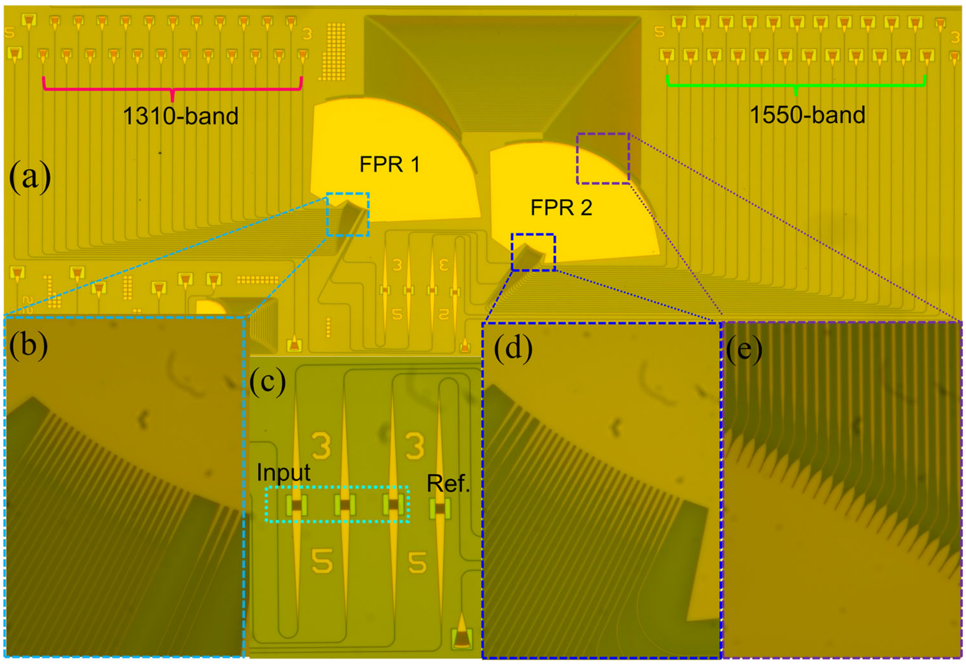


**Figure 7.** a) Microscopic images of the fabricated micro-spectrometer working at dual-wavelength bands. b) Close-up of the 1310 band receiving waveguides and 1550 band input waveguides at the interface of FPR 1. c) Enlarged view of the designed dual-wavelength grating coupler (numbers 3 and 5 denote the 1310 and 1550 bands, respectively). d) Close-up of the 1550 band receiving waveguides and 1310 band input waveguides at the interface of FPR 2. e) Mode converters between FPR and phased array waveguides.

input light, and then is coupled into one of three dual-wavelength grating couplers. After propagating through the AWG, the light is collected at each output port using a single-wavelength grating coupler operating at the 1310 nm band. Then the light is coupled into the second and third dual-wavelength grating couplers, respectively, and collected again at the 23 output ports. Subsequently, the light from the other tunable source with a wavelength ranging from 1500 to 1600 nm is employed and used in a similar manner, the light is collected at each output port using a single-wavelength grating coupler operating at the 1550 nm band. **Figure 8** shows the measured transmission spectra for the reference waveguide with one dual-wavelength grating coupler as input and two single-wavelength grating couplers as outputs. The connecting waveguides between the dual-wavelength input coupler and two single-wavelength output couplers are 2 mm long. The measured transmission losses for the dual-wavelength grating coupler input and single-wavelength grating coupler output are −7.5 dB at $\lambda$ = 1310 nm and −10.4 dB at $\lambda$ = 1550 nm with

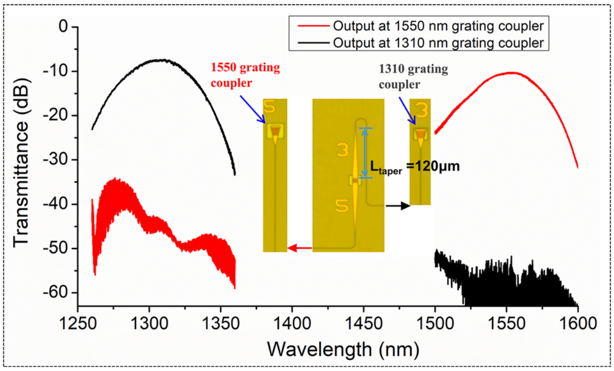


**Figure 8.** Measured transmission spectra of the fabricated reference waveguide with the dual-wavelength grating coupler as input and two single-wavelength grating couplers as output for light input within the dual-wavelength band. The lengths of the connecting waveguides between the dual-wavelength input coupler and two single-wavelength output couplers are 2 mm.

1 dB bandwidths of ≈25 and ≈24.5 nm, respectively. Based on the coupling losses of 3.65 dB at $\lambda$ = 1310 and 5.48 dB at $\lambda$ = 1550 nm for the two single-wavelength output grating couplers (please see Figure S1a,b in the Supporting Information for the detailed derivation) and the propagation losses of 2.5 and 2.0 dB $cm^{-1}$ at $\lambda$ = 1310 and 1550 nm, respectively, for the fabricated connecting waveguides, it can be derived that the measured coupling losses for the dual-wavelength input coupler are 3.35 dB (= 7.5 dB – 2.5 dB $cm^{-1}$ × 0.2 cm–3.65 dB) at $\lambda$ = 1310 nm and 4.52 dB (= 10.4 dB – 2.0 dB $cm^{-1}$ × 0.2 cm – 5.48 dB) at $\lambda$ = 1550 nm. The large difference between the calculated and measured coupling losses for $\lambda$ = 1550 nm is due to the relatively narrow width of 10 μm of the grating region, which results in slightly mode spot size mismatch with an optical fiber mode in the grating width direction, inducing an excess loss, compared to that for $\lambda$ = 1310 nm. Moreover, the high wavelength-band extinction ratio is obtained at each output grating coupler in Figure 8.

**Figures 9** and **10** show the superimposed spectra of all 69 output channels corresponding to their three inputs at the 1310 and 1550 nm bands, respectively. Here each spectrum is normalized to the transmission spectrum of the reference waveguide as shown in Figure 8. One can see that good spectral shapes and uniformities for all 69 output channels are achieved at both wavelength bands owing to the optimized layout design of the fabricated 26 × 26 AWG. At each wavelength band, the obtained effective channel number is 63, while the channel spacings are 0.5 nm at the 1550 nm band and 0.442 nm at the 1310 nm band. The measured central wavelengths at each wavelength band are blueshifted due to the difference between the actual and simulated effective indices in the phase region of AWG. The measured on-chip losses vary from −4.6 to −2.8 dB, and the crosstalk level is less than −18.5 dB at the 1550 nm band, and the on-chip losses range from −7.0 to −3.1 dB and the crosstalk level is less than −16.8 dB at the 1310 nm band. The reason for higher on-chip loss at the 1310 nm band is that, on the one hand, ≈77% (1.326 × 23/39.7) of the free spectral range (FSR) of the designed AWG is occupied at the 1310 nm band while ≈62% (1.5 × 23/55.9) of the FSR is occupied at the 1550 nm band. For a typical AWG, the more the FSR occupied, the higher the loss at the outermost output channel (the maximal loss difference between the outermost and central channels is ≈ 3 dB when the FSR is fully used). On the other hand, in the current design for the 1310 nm band, the angle $\beta^2{}_1$ of the outermost output waveguide is larger than the $\beta^1{}_1$ for the 1550 nm band, which induces more extra loss since each phased array waveguide is designed to point at the center $O_1$ ($O_2$) of the interface between FPR 1 (FPR 2) and input/output waveguides, as shown in the inset of Figure 1. This issue could be addressed by adjusting the designed central wavelength for the 1310 nm band to shift the locations of all output waveguides at the interface of FPR 1 to approach the input waveguides for the 1550 nm band, as shown in Figure 7b. The higher crosstalk level for the 1310 nm band might be attributed to the higher refractive index contrast between the silicon core and oxide cladding compared to the 1550 nm band, causing larger reflection at the interfaces between input (output) waveguides and FPR, and between phased array waveguides and FPR. Moreover, since the three input waveguides correspond to a different input angle $\theta^k{}_i$ in the designed AWG, the excess losses originating from the off-center input are a little different, resulting in the difference of on-chip losses at a given output channel for corresponding three inputs, as observed in adjacent three channels in Figures 9 and 10. This difference, however, can be eliminated by normalization in practical use.

## 4. Discussion

For conventional AWG-based spectrometers,[26,28,47,55,56] the characteristic of large bandwidth and high resolution is usually achieved by cascading a primary coarse wavelength spacing AWG (or coarse wavelength spacing filter) and several secondary fine wavelength spacing AWGs. However, the size of AWG is inversely proportional to its wavelength spacing and proportional to its channel number; it would be very challenging to achieve both high resolution and large bandwidth (bandwidth = channel spacing × channel number) in a limited chip scale. In the proposed micro-spectrometer architecture, one advantage is that using a counter-propagating AWG and a dual-wavelength grating coupler acting as a coarse wavelength separating filter, one AWG can operate at two separate wavelength bands, which increases the working bandwidth of AWG. On the other hand, three time-division-multiplexing inputs with engineered channel spacing for each wavelength band are employed, which enlarges the channel number and decreases the wavelength spacing of AWG with a limited number of output channels and large channel spacing, i.e., using $N$ output ports (photodetectors) at each wavelength band can achieve 3 × ($N$ − 2) channels with a wavelength spacing of 1/3 $\Delta\lambda$ while the designed channel spacing for $N$ output ports is set to $\Delta\lambda$. According to Equation (4), radius $R$ of an AWG is inversely proportional to its channel spacing. Hence, compared to a conventional 1 × 3($N$ − 2) spectrometer with the same wavelength spacing of 1/3 $\Delta\lambda$, the radius $R$ of the fabricated AWG with the channel spacing $\Delta\lambda$ is reduced, which decreases the footprint of the phase region of AWG and, in turn, reduces the size of the micro-spectrometer. The footprint reduction is very beneficial for decreasing the effect of fabrication imperfections on the performance of spectral response of AWG, especially on a high-index-contrast platform. As a result, the proposed architecture achieves a more compact spectrometer with improved work-

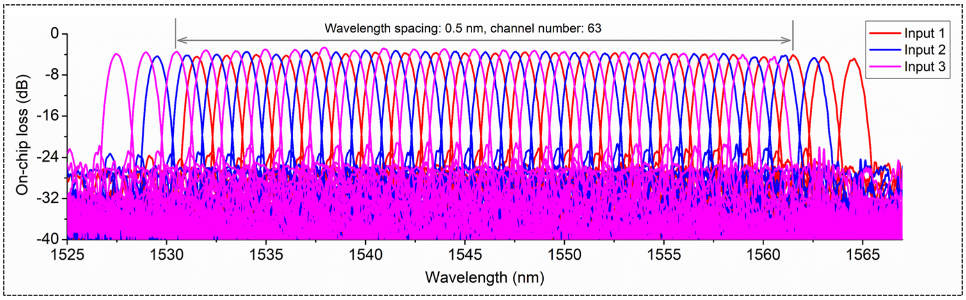


**Figure 9.** Measured transmission spectra of all 23 output channels for corresponding three inputs at the 1550 nm band.

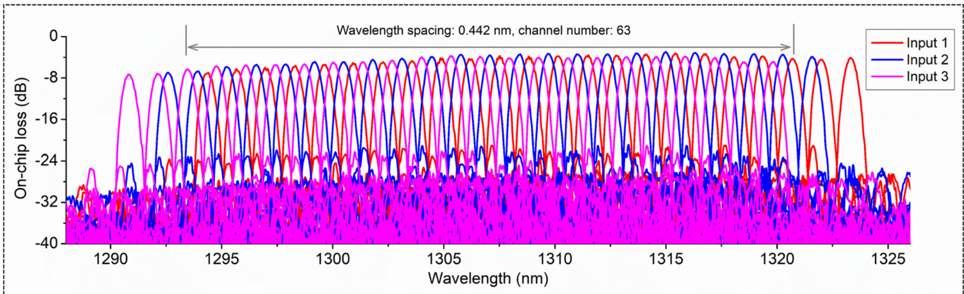


**Figure 10.** Measured transmission spectra of all 23 output channels for corresponding three inputs at the 1310 nm band.

ing bandwidth and fine wavelength spacing. Moreover, thanks to the time-division-multiplexing inputs, the reduced output channel number decreases the required number of photodetectors and, in turn, facilitates the corresponding electrical circuit design (assembly) of spectrometer module, compared to conventional AWG spectrometers.[26,28,47,55,56] **Table 2** shows the performance comparison of SOI-based AWGs (AWG spectrometers) with the fabricated AWG spectrometer.

The fabricated spectrometer employs dual-wavelength input grating couplers to couple light into and single-wavelength grating couplers to couple light out of the chip due to the testing convenience (no need to dice chip compared to edge coupling method) and large alignment tolerance (large mode spot size) of grating couplers, while the coupling losses of the dual-wavelength input grating coupler are 3.35 dB at 1310 nm and 4.52 dB at 1550 nm, and those of single-wavelength output grating couplers are 3.65 dB at 1310 nm and 5.48 dB at 1550 nm, resulting in a total coupling loss of 7 dB at 1310 nm and 10 dB at 1550 nm. For practical applications, the total coupling losses should be substantially decreased. In the future design of the proposed micro-spectrometer, the single-wavelength output grating couplers can be replaced by on-chip integrated germanium-on-silicon photodetectors[57] where the light propagating in output waveguide can be almost fully absorbed, resulting in no coupling loss at output ports. At the same time, the coupling loss of the dual-wavelength input grating coupler can be reduced by further optimizing the grating structure, e.g., adding an extra amorphous silicon layer in the grating region,[58] introducing a high reflection mirror[59] at the bottom of buried oxide layer. Here, as an example, through introducing an extra 140 nm thick silicon layer in the grating region, the simulated coupling losses of the dual-wavelength grating coupler are reduced to 2.0 dB (1.1 dB improvement over the current design) at 1310 nm and 2.06 dB (1.34 dB improvement over the current design) at 1550 nm, as shown in Figure S3 (Supporting Information). Hence, using integrated photodetectors and improved dual-wavelength grating design, the total input and output coupling losses of the improved spectrometer design can be theoretically reduced to below 2.06 dB. On the other hand, for the fabricated micro-spectrometer, three dual-wavelength input grating couplers are time-division-multiplexed, i.e., one of them is excited at a time, which may not be convenient in practical use. In order to facilitate it, as an alternative method, these three dual-wavelength grating couplers can be replaced by one dual-wavelength input grating coupler connected to two on-chip $1 \times 3$ optical switches[60] working at the 1550 and 1310 nm bands, respectively. Then one can measure all three inputs of the AWG spectrometer by controlling the switch status in time sequence at each wavelength band. Based on the above discussion, one improved architecture for the current spectrometer is illustrated in **Figure 11**.

Due to the working principle of wavelength separating, an AWG spectrometer has lower signal-to-noise ratio (SNR) compared to a Fourier transform spectrometer with inherent multiplex advantage,[13] limiting its application to the detection of weak signals. The detected signal strength at one output port of the AWG spectrometer is dependent on the overlap integral of input source with spectral response of this output port. The noise performance (dark current) of employed photodetectors limits the minimum detectable signal strength. For the mentioned one potential application, i.e., FBG sensors, the proposed spectrometer is very suitable since the reflected FPG peaks usually have very low loss after propagating through FBG regions in fiber. For on-chip SD-OCT systems[61] and spectral tissue sensing based on diffuse reflectance spectroscopy,[62] the main limitation of the proposed AWG spectrometer is the total loss, which decreases the SNR of detected signals, resulting in the drawback on the

**Table 2.** State-of-the-art AWG (AWG spectrometers) performance on SOI platform.

| Year[Ref.] | Total (phase region) footprint[a)] [mm$^2$] | Channel spacing [nm] | Channel number | Bandwidth [nm] | Minimum insertion loss[b)] [dB] | Crosstalk[c)] [dB] |
|---|---|---|---|---|---|---|
| 2007[28] | 8 × 8 | 0.2 | 50 | 10 | 17 | −5 |
| 2013[45] | (1.18 × 0.285) | 0.8 | 4 | 3.2 | 2.45 | −17 |
| 2013[46] | 0.23 × 0.53 | 3.2 | 12 | 38.4 | 3 | −20 |
| 2013[47] | 1.1 × 0.78 | 9.6 | 6 | 57.6 | 1.75 | −23.15 |
| 2014[48] | N.A. | 0.8 | 8 | 6.4 | 2.92 | −16.9 |
| 2014[49] | (0.92 × 0.446) | 1.6 | 16 | 25.6 | 2.0 | −23 |
| 2015[50] | (0.43 × 0.35) | 3.2 | 8 | 25.6 | 0.63 | −23 |
| 2017[51] | 1.37 × 0.85 | 0.8 | 8 | 6.4 | 2.8 | −15 |
| 2017[52] | (0.41 × 0.22) | 3.2 | 6 | 19.2 | 2.9 | −24.3 |
| 2017[39] | (0.27 × 0.38) | 3.2 | 15 | 48 | 3.5 | −19 |
| 2018[53] | 0.2 × 0.35 | 6.4 | 4 | 25.6 | 3.5 | −20 |
| 2020[26] | 1.26 × 1.4 (0.65 × 1.06) | 0.4 | 64 | 25.6 | 5.6 | −9 |
| 2020[54] | 2.8 × 1.7 | 0.8 | 16 | 12.8 | 6 | −19.5 |
| 2020[55] | N.A. | 3.68 | 8 | 29.44 | 2.3 | −23.7 |
| 2022[32] | (0.39 × 0.35) | 3.2 | 8 | 25.6 | 2.8 | −25 |
| 2022[56] | 2.3 × 2 | 0.667 | 64 | 42.67 | 5 | −10 |
| This work | 2 × 0.81 (0.6 × 0.58) | 0.5 (0.442) | 63 + 63 | 31.5 + 27.846 | 2.8 (3.1) | −18.5 (−16.8) |

[a)] Total footprint includes phase region and input/output waveguides while phase region footprint does not include input/output waveguides; [b)] Insertion loss is estimated by subtracting a reference waveguide, as illustrated in Figure S4 (Supporting Information); [c)] Crosstalk value is calculated as the difference between the peak power of each channel and the higher contribution of the interference pattern of other signals, as illustrated in Figure S4 (Supporting Information).

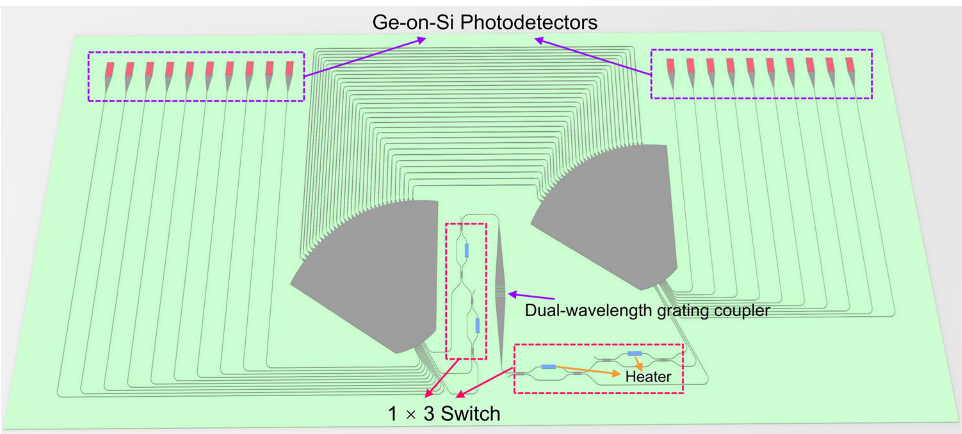


**Figure 11.** Improved architecture of the proposed micro-spectrometer, consisting of one dual-wavelength input grating coupler, two 1 × 3 optical switches working at $\lambda_1$ and $\lambda_2$ bands, respectively, and integrated germanium-on-silicon photodetector array.

detection of wavelength regions with weak intensity; however, an improved design with a theoretical total coupling loss down to 2.06 dB is proposed, as shown in Figure 11.

Moreover, for each wavelength band, a different output waveguide number $N$ and channel spacing $\Delta\lambda$ can be set to meet different requirements in each spectral detection region. In order to further expand the spectral detection range, an array of the proposed spectrometers can be used in parallel, and each spectrometer is designed to work at different $\lambda_1$ and $\lambda_2$ bands. For practical use, one can in turn couple light into each spectrometer or alternatively excite the input of each spectrometer simultaneously through flood illumination.[13]

## 5. Conclusion

In summary, we presented a novel high-resolution and large-bandwidth micro-spectrometer based on a counter-propagating AWG and three dual-wavelength grating couplers. The proposed AWG, working at dual-wavelength bands, has three input waveguides and $N$ output waveguides for each wavelength band. The wavelength channel spacing of input waveguides is 4/3 times that of $N$ output waveguides. Using the time division multiplexing for these three input waveguides, a micro-spectrometer with effective channel number of $3 \times (N - 2)$ and a resolution of 1/3 wavelength spacing of $N$ output waveguides is achieved, only by means of $N$ output waveguides at each wavelength band. In experiment, a micro-spectrometer with 63 channels and channel spacings of 0.5 nm at the 1550 nm band and 0.442 nm at the 1310 nm band is successfully demonstrated by employing a $26 \times 26$ AWG, three dual-wavelength grating couplers, one array of 1550 nm grating couplers and the other array of 1310 nm grating couplers on the SOI platform. The bandwidths of the fabricated spectrometer are 31.5 and 27.85 nm at the 1550 and 1310 nm bands, respectively. The on-chip losses range from −4.6 to −2.8 dB and the crosstalk level is less than −18 dB at the 1550 nm band, and the on-chip losses vary from −7.0 to −3.1 dB and the crosstalk level is less than −16.2 dB at the 1310 nm band, for the obtained 63 channels. The footprint of the fabricated spectrometer is only $2 \times 0.81$ mm$^2$. The proposed micro-spectrometer, having the advantages of ultracompact size, high resolution, large bandwidth, and reduced number of receiving channels (detectors), is very attractive for miniaturized spectroscopic analysis systems.

In addition, the proposed AWG can be redesigned as a $3\times N$ AWG with engineered wavelength spacing for the three input/output ports, which may find the use in optical transceivers for telecom applications such as wavelength division multiplexing/time division multiplexing-passive optical network (WDM/TDM-PON) systems,[63] e.g., as the multiplexer of multiple tunable laser sources where different $N$ wavelength signals are transmitted in different time slots, with only $N$ modulators being required. Conversely, it could also be used in receiving side as the demultiplexer of multiple groups of $N$ wavelength signals with one group at a time slot, and only $N$ photodetectors are needed.

## Supporting Information

Supporting Information is available from the Wiley Online Library or from the author.

## Acknowledgements

This work was supported in part by the Natural Science Foundation of Zhejiang Province under Grant LY22F050011, and in part by the Open Project of the State Key Laboratory of Quantum Optics and Quantum Optics Devices of Shanxi University under Grant No. KF202006.

## Conflict of Interest

The authors declare no conflict of interest.

## Data Availability Statement

The data that support the findings of this study are available from the corresponding author upon reasonable request.

## Keywords

arrayed waveguide gratings, dual-wavelength band grating couplers, high resolution, large bandwidth, silicon-on-insulator, spectrometer on a chip

Received: May 16, 2022
Revised: August 31, 2022
Published online:

[1] H. Ahn, H. Song, D.-M. Shin, K. Kim, J. Choi, *Appl. Spectrosc. Rev.* **2018**, *53*, 264.
[2] B. H. W. Hendriks, A. J. R. Balthasar, G. W. Lucassen, M. van der Voort, M. Mueller, V. V. Pully, T. M. Bydlon, C. Reich, A. T. van Keersop, J. Kortsmit, G. C. Langhout, G. J. van Geffen, *J. Transl. Med.* **2015**, *13*, 380.
[3] N. A. Owens, L. B. Laurentius, M. D. Porter, Q. Li, S. Wang, D. Chatterjee, *Appl. Spectrosc.* **2018**, *72*, 1104.
[4] L. Zhang, J. Chen, C. Ma, W. Li, Z. Qi, N. Xue, *Laser Photonics Rev.* **2021**, *15*, 2100016.
[5] R. Wang, A. Vasiliev, M. Muneeb, A. Malik, S. Sprengel, G. Boehm, M.-C. Amann, I. Šimonytė, A. Vizbaras, K. Vizbaras, R. Baets, G. Roelkens, *Sensors* **2017**, *17*, 1788.
[6] M. Muneeb, A. Vasiliev, A. Ruocco, A. Malik, H. Chen, M. Nedeljkovic, J. S. Penades, L. Cerutti, J. B. Rodriguez, G. Z. Mashanovich, M. K. Smit, E. Tourni, G. Roelkens, *Opt. Express* **2016**, *24*, 9465.
[7] A. Vasiliev, M. Muneeb, J. Allaert, J. V. Campenhout, R. Baets, G. Roelkens, *IEEE J. Sel. Top. Quantum Electron.* **2018**, *24*, 8300207.
[8] Z. Hu, A. Glidle, C. N. Ironside, M. Sorel, M. J. Strain, J. Cooper, H. Yin, *Lab Chip* **2012**, *12*, 2850.
[9] X. Ma, M. Li, J.-J. He, *IEEE Photonics J.* **2013**, *5*, 6600807.
[10] G. Rateni, P. Dario, F. Cavallo, *Sensors* **2017**, *17*, 1453.
[11] E. A. Rank, R. Sentosa, D. J. Harper, M. Salas, A. Gaugutz, D. Seyringer, S. Nevlacsil, A. Maese-Novo, M. Eggeling, P. Muellner, R. Hainberger, M. Sagmeister, J. Kraft, R. A. Leitgeb, W. Drexler, *Light: Sci. Appl.* **2021**, *10*, 6.
[12] G. Reich, *Adv. Drug Delivery Rev.* **2005**, *57*, 1109.
[13] D. González-Andrade, T. T. D. Dinh, S. Guerber, N. Vulliet, S. Cremer, S. Monfray, E. Cassan, D. Marris-Morini, F. Boeuf, P. Cheben, L. Vivien, A. V. Velasco, C. Alonso-Ramos, *Opt. Lett.* **2021**, *46*, 4021.
[14] M. Montesinos-Balleste, Q. Liu, V. Vakarin, J. M. Ramirez, C. Alonso-Ramos, X. L. Roux, J. Frigerio, A. Ballabio, E. Talamas, L. Vivien, G. Isella, D. Marris-Morini, *Sci. Rep.* **2019**, *9*, 14633.
[15] X. Ma, J. Zou, Q. Shao, M. Li, J.-J. He, *Opt. Commun.* **2020**, *456*, 124599.
[16] R. A. Soref, F. De Leonardis, V. M. N. Passaro, Y. Fainman, *J. Lightwave Technol.* **2018**, *36*, 5160.
[17] M. C. Souza, A. Grieco, N. C. Frateschi, Y. Fainman, *Nat. Commun.* **2018**, *9*, 665.
[18] D. Pohl, M. R. Escalé, M. Madi, F. Kaufmann, P. Brotzer, A. Sergeyev, B. Guldimann, P. Giaccari, E. Alberti, U. Meier, R. Grange, *Nat. Photonics* **2020**, *14*, 24.
[19] Z. Xia, A. A. Eftekhar, M. Soltani, B. Momeni, Q. Li, M. Chamanzar, S. Yegnanarayanan, A. Adibi, *Opt. Express* **2011**, *19*, 12356.
[20] B. B. C. Kyotoku, L. Chen, M. Lipson, *Opt. Express* **2010**, *18*, 102.
[21] Z. Zhang, Y. Wang, H. K. Tsang, *ACS Photonics* **2021**, *8*, 1251.
[22] P. Pottier, M. J. Strain, M. Packirisamy, *ACS Photonics* **2014**, *1*, 430.
[23] Z. J. Sun, K. A. McGreer, J. N. Broughton, *IEEE Photonics Technol. Lett.* **1998**, *10*, 90.
[24] D. Geuzebroek, A. V. Rees, E. Klein, K. Lawniczuk, in *IEEE 14th Int. Conf. on Group IV Photonics (GFP)*, IEEE, Piscataway, NJ **2017**, pp. 83–84.
[25] A. v. Wijk, C. R. Doerr, Z. Ali, M. Karabiyik, B. I. Akca, *Opt. Express* **2020**, *28*, 14618.
[26] J. Zou, X. Ma, X. Xia, J. Hu, C. Wang, M. Zhang, T. Lang, J.-J. He, *J. Lightwave Technol.* **2020**, *38*, 4447.
[27] H. Nikbakhth, M. Karabiyik, B. I. Akca, *Opt. Express* **2020**, *28*, 23003.

[28] P. Cheben, J. H. Schmid, A. Delâge, A. Densmore, S. Janz, B. Lamontagne, J. Lapointe, E. Post, P. Waldron, D.-X. Xu, *Opt. Express* **2007**, *15*, 2299.
[29] H. Uetsuka, *IEEE J. Sel. Top. Quantum Electron.* **2004**, *10*, 393.
[30] W. Bogaerts, D. Taillaert, P. Dumon, D. V. Thourhout, R. Baets, E. Pluk, *Opt. Express* **2007**, *15*, 1567.
[31] L. Chen, C. R. Doerr, Y. Chen, in Proc. Opt. Fiber Commun. Conf., OSA Technical Digest, Optical Society of America, Los Angeles, CA, USA **2012**, Paper OW3G.7.
[32] J. Zou, F. Sun, C. Wang, M. Zhang, J. Wang, T. Lang, X. Wang, Z. Le, J.-J. He, *Opt. Laser Technol.* **2022**, *147*, 107656.
[33] S. Chen, X. Fu, J. Wang, Y. Shi, S. He, D. Dai, *J. Lightwave Technol.* **2015**, *33*, 2279.
[34] J. Zou, X. Ma, X. Xia, C. Wang, M. Zhang, J. Hu, X. Wang, J.-J. He, *J. Lightwave Technol.* **2021**, *39*, 2431.
[35] Y. Sano, T. Yoshino, *J. Lightwave Technol.* **2003**, *21*, 132.
[36] A. Trita, G. Vickers, I. Mayordomo, D. van Thourhout, J. Vermeiren, *Proc. SPIE* **2014**, *9133*, 91330D.
[37] R. M. Ruis, A. Leinse, R. Dekker, R. G. Heideman, T. G. van Leeuwen, D. J. Faber, *IEEE J. Sel. Top. Quantum Electron.* **2019**, *25*, 6100109.
[38] G. Song, E. T. Jelly, K. K. Chu, W. Y. Kendall, A. Wax, *Prog. Biomed. Eng.* **2021**, *3*, 032002.
[39] J. Zou, Z. Le, J. Hu, J.-J. He, *Opt. Express* **2017**, *25*, 9963.
[40] G. Roelkens, D. V. Thourhout, R. Baets, *Opt. Express* **2007**, *15*, 10091.
[41] D. Vermeulen, G. Roelkens, J. Brouckaert, D. Van Thourhout, R. Baets, R. Duijin, E. Pluck, G. Van den Hoven, in 34th European Conf. on Optical Communication (ECOC), IEEE, Piscataway, NJ **2008**, paper Tu.3.C.6.
[42] D. González-Andrade, D. Pérez-Galacho, M. Montesinos-Ballester, X. L. Roux, E. Cassan, D. Marris-Morini, P. Cheben, N. Vulliet, S. Monfray, F. Boeuf, L. Vivien, A. V. Velasco, C. Alonso-Ramos, *Opt. Lett.* **2021**, *46*, 617.
[43] L. B. Soldano, E. C. M. Pennings, *J. Lightwave Technol.* **1995**, *13*, 615.
[44] K. Okamoto, A. Sugita, *Electron. Lett.* **1996**, *32*, 1661.
[45] S. Pathak, D. V. Thourhout, W. Bogaerts, *Opt. Lett.* **2013**, *38*, 2961.
[46] K. Okamoto, K. Ishida, *Opt. Lett.* **2013**, *38*, 3530.
[47] M. Muneeb, X. Chen, P. Verheyen, G. Lepage, S. Pathak, E. Ryckeboer, A. Malik, B. Kuyken, M. Nedeljkovic, J. Van Campenhout, G. Z. Mashanovich, G. Roelkens, *Opt. Express* **2013**, *21*, 11659.
[48] J. Wang, Z. Sheng, L. Li, A. Pang, A. Wu, W. Li, X. Wang, S. Zou, M. Qi, F. Gan, *Opt. Express* **2014**, *22*, 9395.
[49] S. Pathak, M. Vanslembrouck, P. Dumon, D. V. Thourhout, P. Verheyen, G. Lepage, P. Absil, W. Bogaerts, *IEEE Photonics Technol. Lett.* **2014**, *26*, 718.
[50] J. Park, G. Kim, H. Park, J. Joo, S. Kim, M.-J. Kwack, *Appl. Opt.* **2015**, *54*, 5597.
[51] H. Okayama, Y. Onawa, D. Shimura, H. Takahashi, H. Yaegashi, H. Sasaki, *Electron. Lett.* **2017**, *53*, 665.
[52] S. Tondini, C. Castellan, M. Mancinelli, C. Kopp, L. Pavesi, *J. Lightwave Technol.* **2017**, *35*, 5134.
[53] Q. Fang, X. Chen, Y. Zhao, J. Hu, H. Chen, C. Qiu, M. Yu, *IEEE Photonics J.* **2018**, *10*, 4900508.
[54] S.-H. Jeong, Y. Onawa, D. Shimura, H. Okayama, T. Aoki, H. Yaegashi, T. Horikawa, T. Nakamura, *J. Lightwave Technol.* **2020**, *38*, 2680.
[55] A. Malik, A. Spott, Y. Wang, E. J. Stanton, J. Peters, J. E. Bowers, *Opt. Lett.* **2020**, *45*, 4551.
[56] Y. Liu, X. Wang, Y. Yao, J. Du, Q. Song, K. Xu, *Opt. Lett.* **2022**, *47*, 1186.
[57] S. Y. Siew, B. Li, F. Gao, H. Y. Zheng, W. Zhang, P. Guo, S. W. Xie, A. Song, B. Dong, L. W. Luo, C. Li, X. Luo, G.-Q. Lo, *J. Lightwave Technol.* **2021**, *39*, 4374.
[58] D. Vermeulen, S. Selvaraja, P. Verheyen, G. Lepage, W. Bogaerts, P. Absil, D. Van Thourhout, G. Roelkens, *Opt. Express* **2010**, *18*, 18278.
[59] A. Melikyan, T. Hu, K. Kim, Y. Baeyens, M. Earnshaw, P. Dong, in Optical Fiber Communication Conf. (OFC) 2019, OSA Technical Digest, Optica Publishing Group, San Diego, CA, USA **2019**, paper Tu2J.5.
[60] K. Suzuki, K. Tanizawa, S. Suda, H. Matsuura, T. Inoue, K. Ikeda, S. Namiki, H. Kawashima, *Opt. Express* **2017**, *25*, 7538.
[61] B. I. Akca, V. D. Nguyen, J. Kalkman, N. Ismail, G. Sengo, F. Dun, A. Driessen, T. G. van Leeuwen, M. Pollnau, K. Wörhoff, R. M. de Ridder, *IEEE J. Sel. Top. Quantum Electron.* **2012**, *18*, 1223.
[62] L. L. de Boer, J. W. Spliethoff, H. J. Sterenborg, T. J. Ruers, *Lasers Med. Sci.* **2017**, *32*, 711.
[63] J.-I. Kani, *IEEE J. Sel. Top. Quantum Electron.* **2010**, *16*, 1290.